Journal of Scientific Computing (2022) 92:16
https://doi.org/10.1007/s10915-022-01862-3

Motion by Mean Curvature with Constraints Using a Modified Allen–Cahn Equation

Soobin Kwak[1] · Hyun Geun Lee[2] · Yibao Li[3] · Junxiang Yang[4] · Chaeyoung Lee[1] · Hyundong Kim[5] · Seungyoon Kang[1] · Junseok Kim[1]

Received: 9 November 2021 / Revised: 26 April 2022 / Accepted: 5 May 2022 /
Published online: 3 June 2022

Abstract
In this article, we present a simple and accurate computational scheme for motion by mean curvature with constraints using a modified Allen–Cahn (AC) equation. The modified AC equation contains a nonlinear source term which enforces the constraints such as volume and average mean curvature. We use a linear convex splitting-type method with Fourier spectral method to numerically solve the modified AC equation. We perform several characteristic computational tests to demonstrate the efficiency and accuracy of the proposed method. The computational results confirm the robust and high performance of the proposed algorithm.

Keywords Motion by mean curvature · Phase-field model · Fourier spectral method · Finite difference method

1 Introduction

In this article, we develop a simple computational scheme for motion by mean curvature with constraints using a modified Allen–Cahn (AC) equation.

$$\frac{\partial \phi(\mathbf{x},t)}{\partial t} = -\frac{F'(\phi(\mathbf{x},t))}{\epsilon^2} + \Delta\phi(\mathbf{x},t) + \alpha \tanh\left(\frac{\beta_T - \beta(\phi)}{\gamma}\right)\frac{\sqrt{2F(\phi(\mathbf{x},t))}}{\epsilon}, \quad (1)$$

where an order parameter is $\phi(\mathbf{x},t)$. Here, $F(\phi) = 0.25(\phi^2-1)^2$, ϵ is a parameter related to the interfacial transition thickness, α is a fidelity strength parameter, γ is a scaling parameter, β_T is the target value, and $\beta(\phi)$ is the current value at time t. In general, a variational energy

✉ Junseok Kim
cfdkim@korea.ac.kr

1 Department of Mathematics, Korea University, Seoul 02841, Republic of Korea

2 Department of Mathematics, Kwangwoon University, Seoul 01897, Republic of Korea

3 School of Mathematics and Statistics, Xi'an Jiaotong University, Xi'an 710049, China

4 School of Computer Science and Engineering, Sun Yat-sen University, Guangzhou 510275, China

5 Institute for the Advanced Study of Human Biology (WPI-ASHBi), Kyoto University Institute for Advanced Study, Kyoto University, Kyoto 6068501, Japan

structure is not available for Eq. (1) because $\beta(\phi)$ is a non-local variable. However, if we use a frozen coefficient method for the term $\alpha \tanh\left(\frac{\beta_T-\beta(\phi)}{\gamma}\right)$, then Eq. (1) can be derived from the following total free energy functional as a gradient flow:

$$\mathcal{E}(\phi) = \int_\Omega \left[\frac{F(\phi)}{\epsilon^2} + \frac{1}{2}|\nabla\phi|^2 + \alpha \tanh\left(\frac{\beta_T - \beta(\phi)}{\gamma}\right) \frac{1}{\sqrt{2}\epsilon} \left(\frac{\phi^3}{3} - \phi\right)\right] d\mathbf{x}. \tag{2}$$

In the frozen coefficient method as used in [35], we keep $\alpha \tanh\left(\frac{\beta_T-\beta(\phi)}{\gamma}\right)$ fixed, and minimize $\mathcal{E}(\phi)$. Then, as a gradient flow, we can obtain Eq. (1) as follows:

$$\frac{\partial\phi}{\partial t} = -\frac{\delta\mathcal{E}(\phi)}{\delta\phi} = -\frac{F'(\phi)}{\epsilon^2} + \Delta\phi + \alpha \tanh\left(\frac{\beta_T - \beta(\phi)}{\gamma}\right) \frac{1-\phi^2}{\sqrt{2}\epsilon}. \tag{3}$$

Note that Eq. (1) becomes the classical AC equation [8] if $\alpha = 0$. The AC equation is a fundamental reaction-diffusion equation that is utilized as a stepping stone in various numerical analysis, such as maximal principle preserving by Zhang et al. [48], and gradient flows by Liu et al. [34].

The triply periodic minimal surface (TPMS) is used to describe the structure or state of substance in nature, e.g., Cidaris rugosa and Dendraster excentricus [38], soap films and soap bubbles, interface between two grains [9], porous fluids and lipid bilayers [36, 40], and chemical bonding [10]. The structure of specific substances such as the above existing in nature can be represented as the intrinsic property of the minimal surface. In recent years, TPMS is applied and numerically researched in fields of cellular or mechanical materials design [1, 2, 6], biological materials design such as porous scaffolds [5, 27, 45, 47], and functionally graded scaffolds [7, 37, 49]. These properties are also applied in structure sciences, and numerically studied by CAD [46], solid T-splines [18], multigrid [33], finite element approach [3, 4, 39, 44], phase-field method [11, 31, 32, 43], etc. In this study, we shall use the initial conditions for TPMS such as Schwarz P, Schwarz D, Schoen G, and Schoen I-WP surfaces on the computational domain Ω to demonstrate the efficiency and accuracy of the proposed method. The contents of this paper are as follows. In Sect. 2, we provide the proposed numerical solution algorithm. In Sect. 3, we present several characteristic computational results. In Sect. 5, conclusions are given.

2 Numerical Solution Algorithm

Now, we present the numerical solution algorithm of the proposed phase-field equation. There have been many numerical methods such as finite difference method [14, 28], finite element method [20, 21], Fourier spectral method [15, 16, 31] for the phase-field models. For simplicity of exposition, we use a Fourier spectral method. Let $\Omega = (l_x, r_x)\times(l_y, r_y)\times(l_z, r_z)$ be the computational domain. Let N_x, N_y, N_z be the number of grid points, and $L_x = r_x - l_x$, $L_y = r_y - l_y$, $L_z = r_z - l_z$ be the length of each direction, respectively. We denote discretized points by $(x_m, y_n, z_o) = (l_x+(m-0.5)h_x,\ l_y+(n-0.5)h_y,\ l_z+(o-0.5)h_z)$ for $1 \le m \le N_x$, $1 \le n \le N_y$, $1 \le o \le N_z$, where $h_x = L_x/N_x$, $h_y = L_y/N_y$, $h_z = L_z/N_z$. For $t_k = k\Delta t$, $\phi(x_m, y_n, z_o, t_k)$ is denoted by ϕ^k_{mno}, where Δt is the temporal step. We apply the linearly stabilized splitting-type method [42] to Eq. (1).

$$\frac{\phi^{k+1}_{mno} - \phi^k_{mno}}{\Delta t} = -\frac{2\phi^{k+1}_{mno}}{\epsilon^2} + (\Delta\phi^{k+1})_{mno} + f^k_{mno}, \tag{4}$$

where

$$f_{mno}^{k} = \frac{3\phi_{mno}^{k} - (\phi_{mno}^{k})^3}{\epsilon^2} + \alpha(\beta_T - \beta(\phi^k))\frac{\sqrt{2F(\phi_{mno}^{k})}}{\epsilon}. \tag{5}$$

For the given data $\{\phi_{mno}^{k} \mid m = 1, \ldots, N_x,\ n = 1, \ldots, N_y,\ o = 1, \ldots, N_z\}$ the discrete Fourier transform is defined as

$$\hat{\phi}_{pqr}^{k} = \sum_{m=1}^{N_x}\sum_{n=1}^{N_y}\sum_{o=1}^{N_z}\phi_{mno}^{k} e^{-i(\xi_p x_m + \eta_q y_n + \omega_r z_o)}, \tag{6}$$

$$-\frac{N_x}{2} + 1 \le p \le \frac{N_x}{2},\ -\frac{N_y}{2} + 1 \le q \le \frac{N_y}{2},\ -\frac{N_z}{2} + 1 \le r \le \frac{N_z}{2}, \tag{7}$$

where $\xi_p = 2\pi p/L_x$, $\eta_q = 2\pi q/L_y$, $\omega_r = 2\pi r/L_z$. The inverse discrete Fourier transform is

$$\phi_{mno}^{k} = \sum_{p=-\frac{N_x}{2}+1}^{\frac{N_x}{2}}\sum_{q=-\frac{N_y}{2}+1}^{\frac{N_y}{2}}\sum_{r=-\frac{N_z}{2}+1}^{\frac{N_z}{2}}\hat{\phi}_{pqr}^{k}\frac{e^{i(\xi_p x_m + \eta_q y_n + \omega_r z_o)}}{N_x N_y N_z}. \tag{8}$$

Let $\phi(x, y, z, t)$ be continuous version of ϕ_{mno}^{k}. Therefore, we can obtain the following results:

$$\frac{\partial^2\phi(x,y,z,t)}{\partial x^2} = -\sum_{p=-\frac{N_x}{2}+1}^{\frac{N_x}{2}}\sum_{q=-\frac{N_y}{2}+1}^{\frac{N_y}{2}}\sum_{r=-\frac{N_z}{2}+1}^{\frac{N_z}{2}}\xi_p^2\hat{\phi}(\xi_p,\eta_q,\omega_r,t)\frac{e^{i(\xi_p x+\eta_q y+\omega_r z)}}{N_x N_y N_z}, \tag{9}$$

$$\frac{\partial^2\phi(x,y,z,t)}{\partial y^2} = -\sum_{p=-\frac{N_x}{2}+1}^{\frac{N_x}{2}}\sum_{q=-\frac{N_y}{2}+1}^{\frac{N_y}{2}}\sum_{r=-\frac{N_z}{2}+1}^{\frac{N_z}{2}}\eta_q^2\hat{\phi}(\xi_p,\eta_q,\omega_r,t)\frac{e^{i(\xi_p x+\eta_q y+\omega_r z)}}{N_x N_y N_z}, \tag{10}$$

$$\frac{\partial^2\phi(x,y,z,t)}{\partial z^2} = -\sum_{p=-\frac{N_x}{2}+1}^{\frac{N_x}{2}}\sum_{q=-\frac{N_y}{2}+1}^{\frac{N_y}{2}}\sum_{r=-\frac{N_z}{2}+1}^{\frac{N_z}{2}}\omega_r^2\hat{\phi}(\xi_p,\eta_q,\omega_r,t)\frac{e^{i(\xi_p x+\eta_q y+\omega_r z)}}{N_x N_y N_z} \tag{11}$$

and

$$\Delta\phi(x,y,z,t) = \sum_{p=-\frac{N_x}{2}+1}^{\frac{N_x}{2}}\sum_{q=-\frac{N_y}{2}+1}^{\frac{N_y}{2}}\sum_{r=-\frac{N_z}{2}+1}^{\frac{N_z}{2}}\widehat{\Delta\phi}(\xi_p,\eta_q,\omega_r,t)\frac{e^{i(\xi_p x+\eta_q y+\omega_r z)}}{N_x N_y N_z} \tag{12}$$

$$= \sum_{p=-\frac{N_x}{2}+1}^{\frac{N_x}{2}}\sum_{q=-\frac{N_y}{2}+1}^{\frac{N_y}{2}}\sum_{r=-\frac{N_z}{2}+1}^{\frac{N_z}{2}} -(\xi_p^2+\eta_q^2+\omega_r^2)\hat{\phi}(\xi_p,\eta_q,\omega_r,t)\frac{e^{i(\xi_p x+\eta_q y+\omega_r z)}}{N_x N_y N_z},$$

where the left-hand side is the definition of the inverse Fourier transform and the right-hand side is the sum of Eqs. (9)–(11). After applying Eqs. (8) and (12), we have

$$\frac{\hat{\phi}^{k+1}_{pqr} - \hat{\phi}^{k}_{pqr}}{\Delta t} = -\frac{2\hat{\phi}^{k+1}_{pqr}}{\epsilon^2} - (\xi_p^2 + \eta_q^2 + \omega_r^2)\hat{\phi}^{k+1}_{pqr} + \hat{f}^{k}_{pqr}. \tag{13}$$

Equation (13) can be rewritten as

$$\hat{\phi}^{k+1}_{pqr} = \frac{\hat{\phi}^{k}_{pqr}/\Delta t + \hat{f}^{k}_{pqr}}{1/\Delta t + 2/\epsilon^2 + \xi_p^2 + \eta_q^2 + \omega_r^2}. \tag{14}$$

Then, the updated numerical solution ϕ^{k+1}_{mno} can be computed using Eq. (8):

$$\phi^{k+1}_{mno} = \sum_{p=-\frac{N_x}{2}+1}^{\frac{N_x}{2}} \sum_{q=-\frac{N_y}{2}+1}^{\frac{N_y}{2}} \sum_{r=-\frac{N_z}{2}+1}^{\frac{N_z}{2}} \hat{\phi}^{k+1}_{pqr} \frac{e^{i(\xi_p x_m + \eta_q y_n + \omega_r z_o)}}{N_x N_y N_z}. \tag{15}$$

Next, the discrete surface area and surface averaged mean curvature are defined. The normal vector of the top right back vertex of the cell is defined as

$$\mathbf{m}_{i+\frac{1}{2},j+\frac{1}{2},k+\frac{1}{2}} = \left(m^x_{i+\frac{1}{2},j+\frac{1}{2},k+\frac{1}{2}}, m^y_{i+\frac{1}{2},j+\frac{1}{2},k+\frac{1}{2}}, m^z_{i+\frac{1}{2},j+\frac{1}{2},k+\frac{1}{2}} \right),$$

where

$$\begin{aligned} m^x_{i+\frac{1}{2},j+\frac{1}{2},k+\frac{1}{2}} = & \frac{\phi_{i+1,j,k} + \phi_{i+1,j,k+1} + \phi_{i+1,j+1,k} + \phi_{i+1,j+1,k+1}}{4h} \\ & - \frac{\phi_{ijk} + \phi_{i,j,k+1} + \phi_{i,j+1,k} + \phi_{i,j+1,k+1}}{4h} \end{aligned}$$

and the other terms are defined similarly. The mean curvature $\kappa(\phi_{ijk})$ specified as follows is calculated from the cell-center of the vertex-centered normals

$$\begin{aligned} \kappa(\phi_{ijk}) &= \nabla_d \cdot \left(\frac{\mathbf{m}}{|\,\mathbf{m}\,|} \right)_{ijk} \\ &= \frac{1}{4h} \left(\frac{(m^x + m^y + m^z)_{i+\frac{1}{2},j+\frac{1}{2},k+\frac{1}{2}}}{|\,\mathbf{m}_{i+\frac{1}{2},j+\frac{1}{2},k+\frac{1}{2}}\,|} + \frac{(m^x + m^y - m^z)_{i+\frac{1}{2},j+\frac{1}{2},k-\frac{1}{2}}}{|\,\mathbf{m}_{i+\frac{1}{2},j+\frac{1}{2},k-\frac{1}{2}}\,|} \right. \\ &\quad + \frac{(m^x - m^y + m^z)_{i+\frac{1}{2},j-\frac{1}{2},k+\frac{1}{2}}}{|\,\mathbf{m}_{i+\frac{1}{2},j-\frac{1}{2},k+\frac{1}{2}}\,|} + \frac{(m^x - m^y - m^z)_{i+\frac{1}{2},j-\frac{1}{2},k-\frac{1}{2}}}{|\,\mathbf{m}_{i+\frac{1}{2},j-\frac{1}{2},k-\frac{1}{2}}\,|} \\ &\quad - \frac{(m^x - m^y - m^z)_{i-\frac{1}{2},j+\frac{1}{2},k+\frac{1}{2}}}{|\,\mathbf{m}_{i-\frac{1}{2},j+\frac{1}{2},k+\frac{1}{2}}\,|} - \frac{(m^x - m^y + m^z)_{i-\frac{1}{2},j+\frac{1}{2},k-\frac{1}{2}}}{|\,\mathbf{m}_{i-\frac{1}{2},j+\frac{1}{2},k-\frac{1}{2}}\,|} \\ &\quad \left. - \frac{(m^x + m^y - m^z)_{i-\frac{1}{2},j-\frac{1}{2},k+\frac{1}{2}}}{|\,\mathbf{m}_{i-\frac{1}{2},j-\frac{1}{2},k+\frac{1}{2}}\,|} - \frac{(m^x + m^y + m^z)_{i-\frac{1}{2},j-\frac{1}{2},k-\frac{1}{2}}}{|\,\mathbf{m}_{i-\frac{1}{2},j-\frac{1}{2},k-\frac{1}{2}}\,|} \right). \end{aligned}$$

The cell-centered normal expressed as follows is the average of vertex normals,

$$\nabla_d \phi_{ijk} = \left(\frac{\phi_{i-2,j,k} - 8\phi_{i-1,j,k} + 8\phi_{i+1,j,k} - \phi_{i+2,j,k}}{12h}, \right.$$
$$\frac{\phi_{i,j-2,k} - 8\phi_{i,j-1,k} + 8\phi_{i,j+1,k} - \phi_{i,j+2,k}}{12h},$$
$$\left. \frac{\phi_{i,j,k-2} - 8\phi_{i,j,k-1} + 8\phi_{i,j,k+1} - \phi_{i,j,k+2}}{12h} \right).$$

Therefore, the discretized surface area of $\mathscr{A}$[29] is

$$\sum_{i=1}^{N_x} \sum_{j=1}^{N_y} \sum_{k=1}^{N_z} \frac{3\sqrt{2}\epsilon}{4} |\ \nabla_d \phi_{ijk}\ |^2 h^3 \approx \mathscr{A}(\phi)$$

and

$$-\frac{\sum_{i=1}^{N_x} \sum_{j=1}^{N_y} \sum_{k=1}^{N_z} 0.75\sqrt{2}\epsilon\kappa(\phi_{ijk}) |\ \nabla_d \phi_{ijk}\ |^2 h^3}{\mathscr{A}(\phi)} \approx \bar{\kappa}(\phi)$$

is the averaged mean curvature. The target value β_T can be set as a surface area value or mean curvature, and $\beta(\phi)$ is $\mathscr{A}(\phi)$ and $\bar{\kappa}(\phi)$, respectively. The discrete l_2-norm is defined as

$$||\ \phi\ ||_2 = \sqrt{\sum_{i=1}^{N_x} \sum_{j=1}^{N_y} \sum_{k=1}^{N_z} \frac{\phi_{ijk}^2}{N_x N_y N_z}}.$$

3 Computational Results

3.1 Spherical Surface

We first consider the term, $\tanh\left[(\beta_T - \beta(\phi))/\gamma\right]$, in Eq. (1) and its effect of the evolutionary dynamics. Figure 1 shows the profiles of the hyperbolic tangent function $\tanh(x/\gamma)$ with different γ parameter values. It can be observed that the transition width increases as the value of γ increases.

Figure 2 shows the effect of γ value on the evolutionary dynamics. In $\Omega = (-1.5, 1.5) \times (-1.5, 1.5) \times (-1.5, 1.5)$, the initial conditions used are

$$\phi(x, y, z, 0) = \tanh\left(\frac{1 - \sqrt{x^2 + y^2 + z^2}}{\sqrt{2}\epsilon} \right).$$

Here, $N_x = 128$, $N_y = 128$, $N_z = 128$, $\Delta t = 0.001$, and $\epsilon = 0.034$ are used. We set $\beta(\phi) = 0.5 \sum_{i=1}^{N_x} \sum_{j=1}^{N_y} \sum_{k=1}^{N_z} (1 + \phi_{ijk}) h^3$ and $\beta_T = (4/3)\pi(1.2)^3$ which is the volume of the sphere of radius 1.2. It can be observed that if γ is large, then the evolution of the volume $\beta(\phi)$ oscillates around the target volume. If γ is small, then the evolution of the volume $\beta(\phi)$ is very slowly approaching the target volume. The value $\gamma = 0.5$ gives an appropriate result.

For stable and fast computation, an appropriate γ value should be selected to obtain the computational results without oscillation as shown in Fig. 2. To find a suitable γ value, let $\lambda = |\ \beta_T - \beta(\phi^0)\ | / \gamma$. Figure 3 shows $\tanh(\lambda)$ values for the three different $\gamma = 0.05,\ 0.5$, and 5 values. When $\gamma = 0.5$, we have $\tanh(\lambda) = 0.999983371996023$. Therefore, an appropriate γ value can be chosen as $\lambda = \tanh^{-1}(0.99999)$, i.e., $\gamma = |\ \beta_T - \beta(\phi^0)\ | / \tanh^{-1}(0.99999)$.

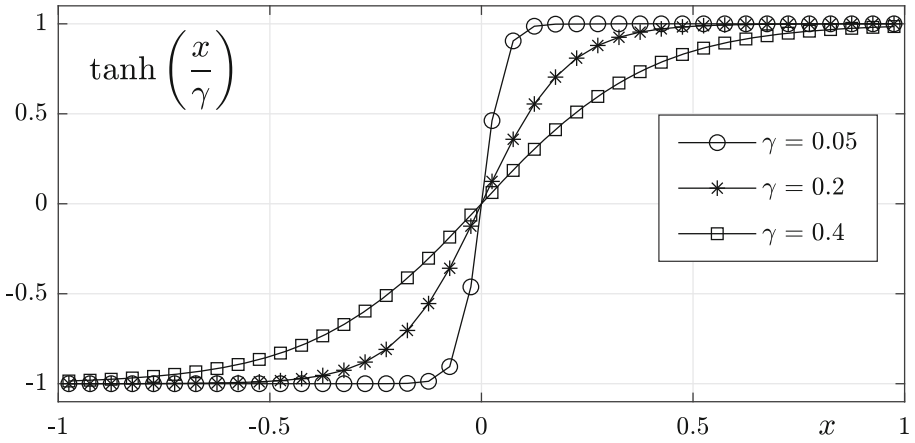

Fig. 1 Effect of γ parameter on the profile of the hyperbolic tangent function, $\tanh(x/\gamma)$. Here, $\gamma = 0.05$, 0.2, and 0.4 are used

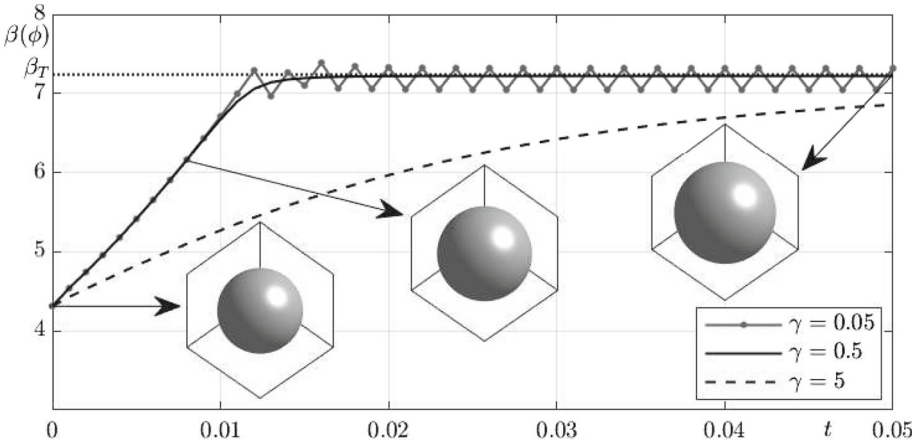

Fig. 2 Effect of γ value on the evolutionary dynamics of the volume $\beta(\phi)$

Figure 4 shows the effect of α value on the evolutionary dynamics. All the parameter values are the same to the previous test except α and γ values. $\gamma = 0.5$ is fixed, and α value changes. We can observe that if α is large, then the evolution of the volume $\beta(\phi)$ oscillates around the target volume. If α is small, then the evolution of the volume $\beta(\phi)$ is very slowly approaching the target volume. The value $\alpha = 50$ gives an appropriate result.

In Fig. 5, the evolution of the curvature is observed by setting the target value β as the curvature. The initial conditions and parameters we used are as follows:

$$\phi(x, y, z, 0) = \tanh\left(\frac{\max(\min(\min(0.8 - |x|, 0.8 - |y|), 0.8 - |z|), -0.8)}{\sqrt{2}\epsilon}\right),$$

$\Omega = (-1, 1) \times (-1, 1) \times (-1, 1)$, $N_x = 128$, $N_y = 128$, $N_z = 128$, $\Delta t = 0.001$ and $\epsilon = 0.0225$. We set $\beta(\phi) = \bar{\kappa}(\phi)$ and $\beta_T = 4$. The simulation stops when $||\phi^{n+1} - \phi^n||_2 < tol$. Here, the tolerance tol is used as 1.0e−3. We confirmed that as the curvature evolves, the cube of the initial state changes to a spherical surface.

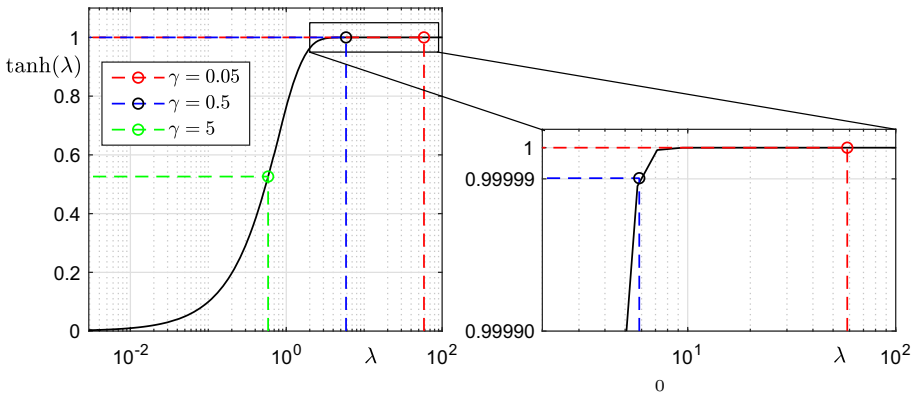

Fig. 3 Values of tanh(λ) for different λ values. Here, $\lambda = | \beta_T - \beta(\phi^0) | / \gamma$ for the three different $\gamma = 0.05,\ 0.5$, and 5 values

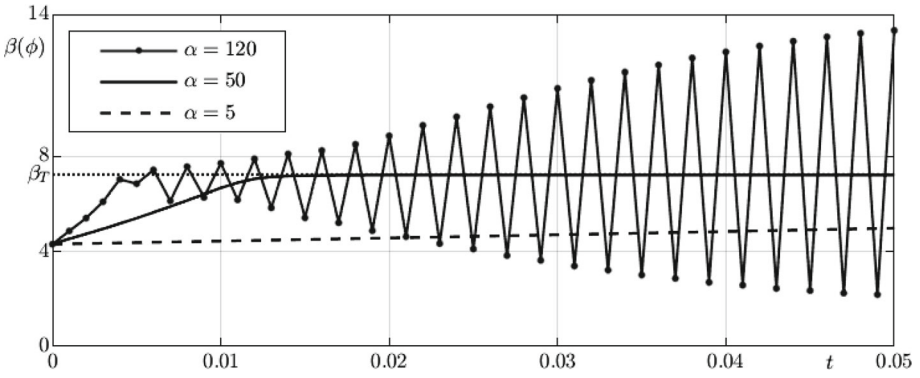

Fig. 4 Effect of α value on the evolutionary dynamics of the volume $\beta(\phi)$

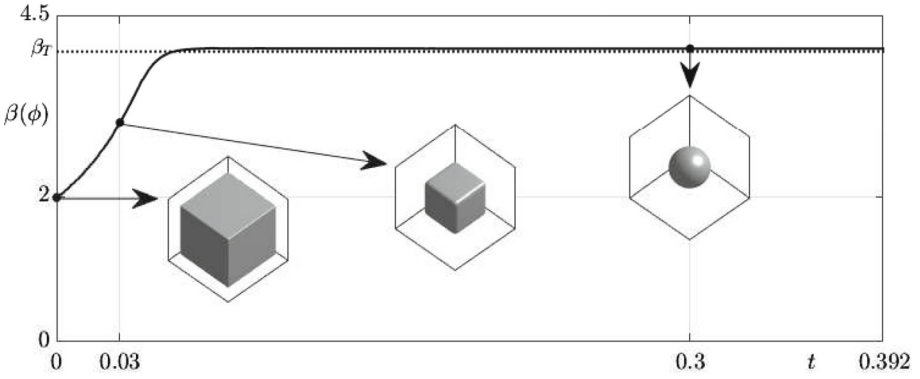

Fig. 5 Evolution of the curvature for cube

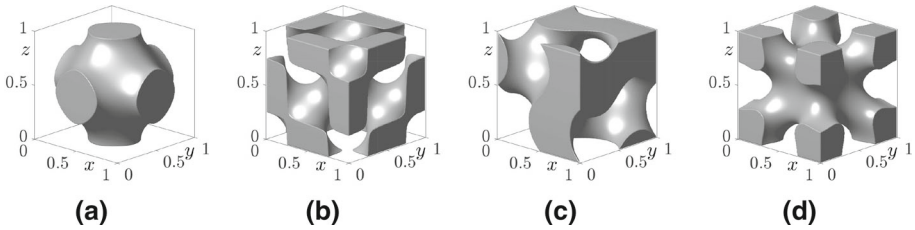

Fig. 6 Initial configurations of **a** Schwarz P, **b** Schwarz D, **c** Schoen G, and **d** Schoen I-WP surfaces

3.2 Triply Periodic Constant Mean Curvature Surfaces

Next, we present generations of triply periodic constant mean curvature surfaces with prescribed volume and mean curvature from the periodic nodal surface (PNS) approximations of the Schwarz P, Schwarz D, Schoen G, and Schoen I-WP surfaces [22]. We take the following initial conditions for the Schwarz P, Schwarz D, Schoen G, and Schoen I-WP surfaces on the computational domain $\Omega = (0, 1) \times (0, 1) \times (0, 1)$.

$$P(x, y, z) = -\tanh\left(\frac{\cos 2\pi x + \cos 2\pi y + \cos 2\pi z}{4\sqrt{2}\epsilon}\right), \tag{16}$$

$$D(x, y, z) = -\tanh\left(\frac{\cos 2\pi x \cos 2\pi y \cos 2\pi z - \sin 2\pi x \sin 2\pi y \sin 2\pi z}{4\sqrt{2}\epsilon}\right), \tag{17}$$

$$G(x, y, z) = -\tanh\left(\frac{\sin 2\pi x \cos 2\pi y + \sin 2\pi y \cos 2\pi z + \sin 2\pi z \cos 2\pi x}{4\sqrt{2}\epsilon}\right),$$

$$I\text{-}WP(x, y, z) = -\tanh\Big[\big(2\cos 2\pi x \cos 2\pi y + 2\cos 2\pi x \cos 2\pi y \tag{18}$$

$$+ 2\cos 2\pi x \cos 2\pi y - \cos 4\pi x - \cos 4\pi x - \cos 4\pi x\big)/\big(4\sqrt{2}\epsilon\big)\Big]. \tag{19}$$

Here, $N_x = N_y = N_z = 200$, $h = 1/200$, $\Delta t = 0.001$, $\epsilon = 0.01$, $\alpha = 50$, and $\gamma = 0.05$ are used. Figure 6a–d illustrate the initial configurations of Eqs. (16), (17), (18), and (19), respectively.

First, we consider $\beta(\phi)$ as the volume of the phase. It means that the numerical solution converges towards the prescribed target volume β_T. We set the stopping criterion as $||\phi^{n+1} - \phi^n||_2 < tol$, and $tol = 1.0\text{e}{-3}$. Figure 7 shows the numerical results of the three surfaces for three different target volumes: $\beta_T = 0.5,\ 0.35$, and 0.65 (from top to bottom). The numerical results indicate that we can generate a family of the Schwarz P, Schwarz D, Schoen G, and Schoen I-WP surfaces with prescribed target volumes β_T.

The proposed numerical solutions can be manufactured as a real-life 3D model using a 3D printer. When a 3D digital model is inserted to a 3D printer, the model is sliced into piles of 2D layers. Then, the 3D printer prints out the 2D layers from bottom to top, forming a 3D build. If a top layer is overwhelming in size compared to the bottom layer, there is a chance of the top layer falling down. Cases like these require supporting pillars for the top layer. In our numerical results, Schwarz D, Schoen G, and Schoen I-WP surfaces required additional supporting pillars for 3D printing. Figure 8 exhibits the manufactured models of previously described numerical solutions via 3D printing. These 3D printed TPMS can be widely used in various fields, such as mechanical materials design, bio-scaffold design, and functionally graded scaffold design.

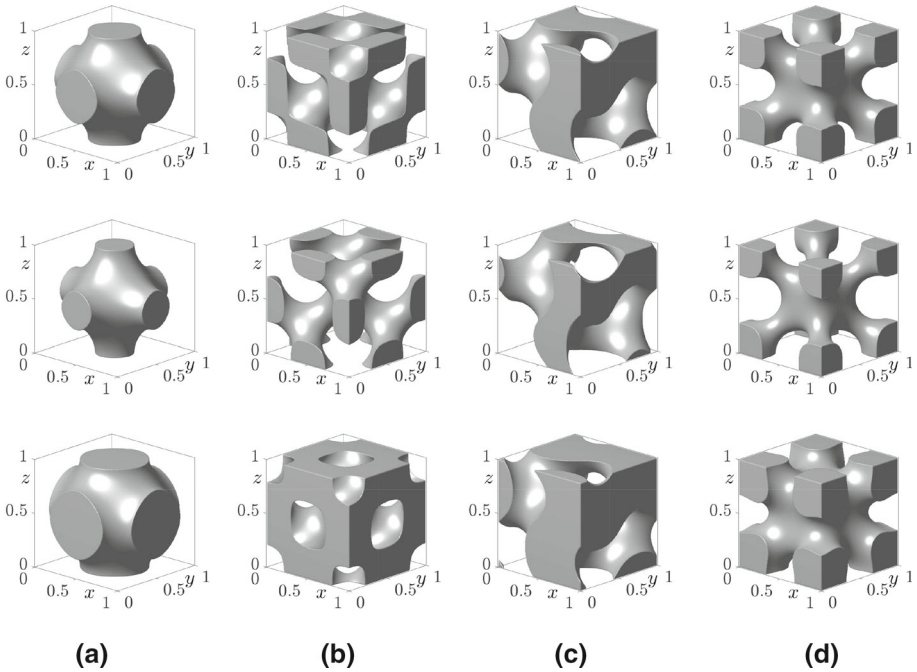

Fig. 7 Final configurations of **a** Schwarz P, **b** Schwarz D, **c** Schoen G, and **d** Schoen I-WP surfaces. From top to bottom, target volumes are $\beta_T = 0.5,\ 0.35$, and 0.65, respectively

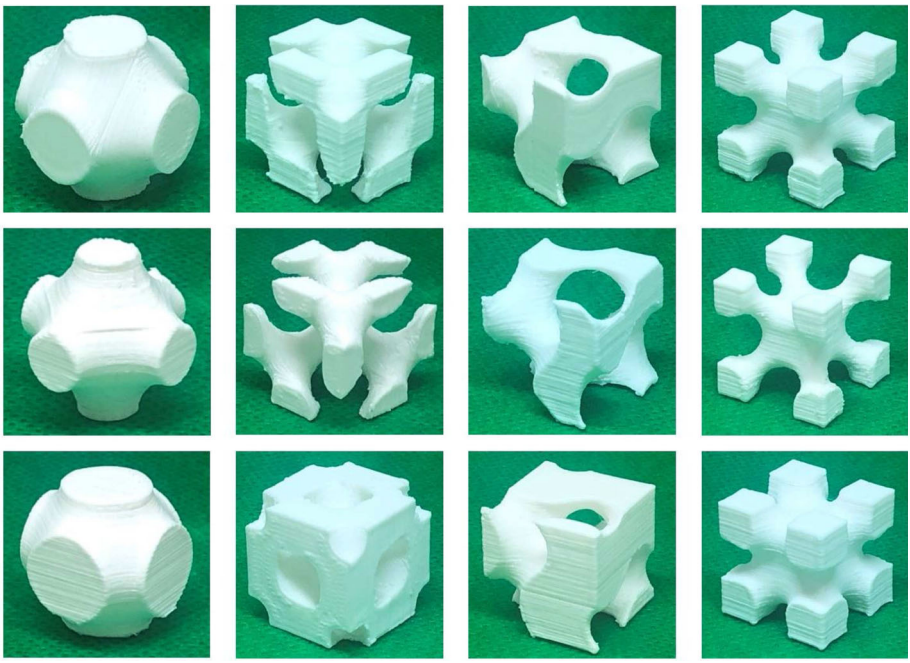

Fig. 8 3D printed model of numerical results shown in Fig. 7

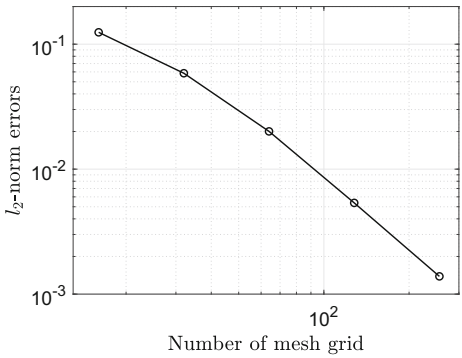

Fig. 9 Convergence of spectral-order accurate method in space

Table 1 l_2-norm errors and convergence rates in time

$(\Delta t, \Delta t/2)$	l_2-norm error	Rate
(2.5000e−7, 1.2500e−7)	3.3452e−5	
(1.2500e−7, 6.2500e−8)	1.6988e−5	0.98
(6.2500e−8, 3.1250e−8)	8.5610e−6	0.99
(3.1250e−8, 1.5625e−8)	4.2975e−6	0.99

We conduct the convergence test in time and space using the initial condition (16). The proposed method is first-order accurate in time and spectral-order accurate in space. For the convergence rate in time, the target volume is taken as $\beta_T = 0.65$ and the final time is fixed as $T = N_t \Delta t = 2.5\text{e}{-6}$, and other parameters not mentioned are used as described above. The discrete error is defined as $E_{ijk}^{(\Delta t, \Delta t/2)} = \phi_{ijk}^{N_t} - \phi_{ijk}^{2N_t}$ and its discrete l_2-norm is used. The rate of convergence is defined as $\log_2 \left(||E^{(\Delta t, \Delta t/2)}||_2 / ||E^{(\Delta t/2, \Delta t/4)}||_2 \right)$. As the temporal step size Δt is reduced by twice, the rate of convergence is listed in Table 1. For the convergence rate in space, we take $\Delta t = 1.0\text{e}{-8}$, $T = 1.0\text{e}{-7}$, and $\beta_T = 0.65$. The discrete error is defined as $E_{ijk}^{(h,h/2)} = \phi_{ijk}^{h} - 0.125(\phi_{ijk}^{h/2} + \phi_{i+1,jk}^{h/2} + \phi_{i,j+1,k}^{h/2} + \phi_{i+1,j+1,k}^{h/2} + \phi_{ij,k+1}^{h/2} + \phi_{i+1,j,k+1}^{h/2} + \phi_{i,j+1,k+1}^{h/2} + \phi_{i+1,j+1,k+1}^{h/2})$. As doubling the number of mesh grid $N = N_x = N_y = N_z$ from 1 to 512, we observe the spatial spectral accuracy [25] as shown Fig. 9.

We compute the mean curvatures, surface areas, and CPU times while changing the target volumes from 0.35 to 0.65 with 0.05 interval. Then, the computational results of Schwarz P, Schwarz D, and Schoen G are compared with the results reported by Jung et al. [26], which were obtained from the level-set method. Here, the surface averaged mean curvature is defined as $0.5\bar{\kappa}(\phi)$ in order to compare with the test of the reference. Figure 10a, b show the mean curvature and the surface area according to the target volume, respectively. The results in Fig. 10 show that our proposed method agrees well with those from the method of Jung et al. Figure 10c shows the CPU times it takes to carry out each computation with $tol = 1.0\text{e}{-6}$. For Schwarz P and Schwarz D, they take about 36 min and about 15 min respectively. Meanwhile, the method proposed in Jung et al. [26] described 29 h and 30 h. Note that Jung et al. utilized 4 node parallel calculations on the Opteron cluster, while we use a single computer, an Intel(R) Core(TM) i7-10700 CPU@2.90GHz with 32GB memory, and MATLAB R2020b software. From the results, our proposed method is extremely fast, specifically, the computational cost is reduced by more than 48 orders.

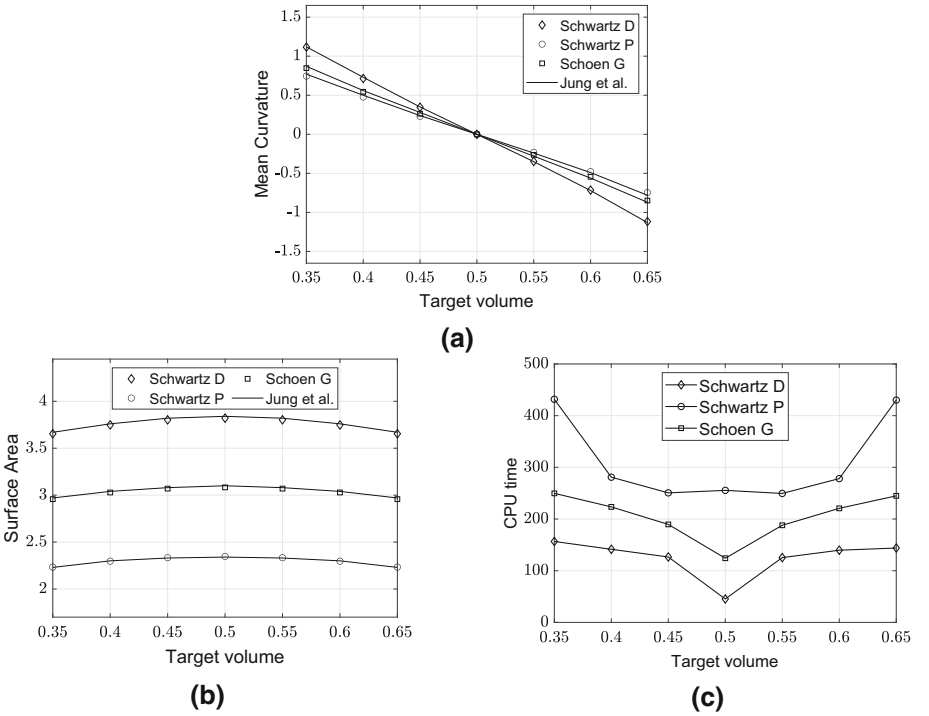

Fig. 10 Volume $\beta(\phi)$: For the local equilibrium of the Schwarz P, Schwarz D, and Schoen G surfaces, volume fraction versus **a** mean curvature, **b** surface area, and **c** CPU time (s)

Second, we consider $\beta(\phi)$ as the averaged mean curvature of the surface. All the parameters are the same to the previous test except the definition of the constraint $\beta(\phi)$. As shown in Fig. 11, the initial condition is taken as

$$\phi(x, y, z, 0) = \begin{cases} 1 & \text{if } (|x| < 0.25,\ |y| < 0.25) \text{ or } (|y| < 0.25,\ |z| < 0.25) \text{ or} \\ & (|x| < 0.25,\ |z| < 0.25), \\ -1 & \text{otherwise} \end{cases} \tag{20}$$

on the computational domain $\Omega = (-0.5, 0.5) \times (-0.5, 0.5) \times (-0.5, 0.5)$. Here, $N_x = N_y = N_z = 100$, $h = 1/100$, $\Delta t = 0.001$, $\epsilon = 0.01$, $\alpha = -50$, $\gamma = 0.1$, and $tol = 1.0\text{e}{-4}$ are used. Unlike the previous test where the target value is set to the volume, α is a negative value because the curvature is inversely proportional to the volume.

The numerical tests are performed using three different target values $\beta_T = 0,\ -1$, and 1. The temporal evolutions are shown in Fig. 13 whose target values are $\beta_T = 0,\ -1$, and 1 from top to bottom. The final times of Fig. 13d are $t = 492\Delta t,\ 636\Delta t$, and $636\Delta t$, respectively.

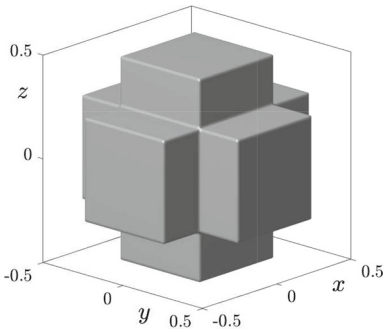

Fig. 11 Initial configuration of Eq. (20)

4 Discussion

In this paper, we focused on a new phase-field model and its simple numerical method. We may consider a higher-order numerical scheme and an adaptive algorithm for improved accuracy and robustness of the algorithm.

4.1 Crank–Nicolson Scheme

The AC equation has been long studied to approximate the mean curvature motion, as the interfacial width parameter approaches to 0. In the convergence estimate for the AC equation, the convergence constant better depends on ϵ^{-1} in a polynomial pattern, instead of an exponential growth one [19]. It is better to have higher-order numerical schemes for accurate computations. The second-order accurate stable numerical methods have been developed, for example, [17, 23, 41]. For a higher-order numerical scheme for Eq. (1), we may consider a Crank–Nicolson type finite difference method as follows:

$$\begin{aligned}\frac{\phi_{mno}^{k+1}-\phi_{mno}^{k}}{\Delta t} = &-\frac{F'(\phi_{mno}^{k+1})}{2\epsilon^2}+\frac{1}{2}\Delta_h\phi_{mno}^{k+1}+\frac{\alpha}{2}\tanh\left(\frac{\beta_T-\beta(\phi^{k+\frac{1}{2}})}{\gamma}\right)\frac{\sqrt{2F(\phi_{mno}^{k+1})}}{\epsilon}\\ &-\frac{F'(\phi_{mno}^{k})}{2\epsilon^2}+\frac{1}{2}\Delta_h\phi_{mno}^{k}+\frac{\alpha}{2}\tanh\left(\frac{\beta_T-\beta(\phi^{k+\frac{1}{2}})}{\gamma}\right)\frac{\sqrt{2F(\phi_{mno}^{k})}}{\epsilon},\end{aligned}$$

where $\Delta_h\phi_{mno}^k = (\phi_{m+1,no}^k + \phi_{m-1,no}^k + \phi_{m,n+1,o}^k + \phi_{m,n-1,o}^k + \phi_{mn,o+1}^k + \phi_{mn,o-1}^k - 6\phi_{mno}^k)/h^2$ and $\phi^{k+\frac{1}{2}} = (3\phi^k - \phi^{k-1})/2$. $\phi^{\frac{1}{2}}$ can be obtained from an iterative update. The implicit part of the discrete equation can be solved using a nonlinear multigrid method [28]. We note that if the governing equation can be derived from an energy functional, then we may consider a second-order numerical scheme with energy stability for the equation as done in [24].

4.2 Adaptive Algorithm

Some numerical results show that oscillations occur for some choices of the parameters. For further improvement of the proposed algorithm, we can consider an adaptive methodology which is robust with respect to model parameters. The adaptive algorithm is as follows. We

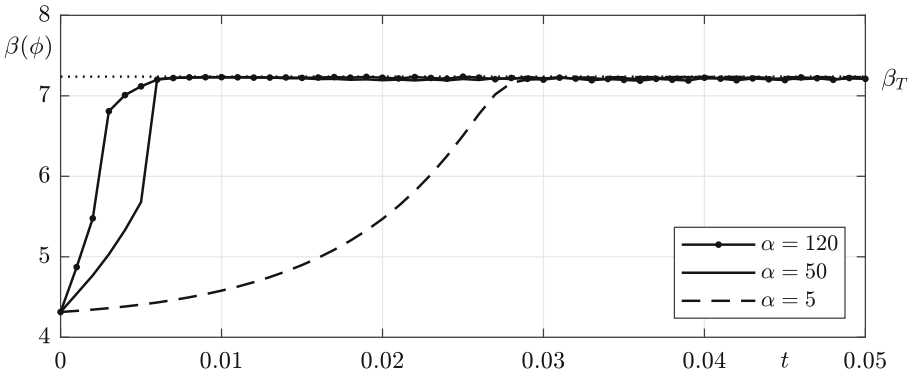

Fig. 12 Temporal volution of the volume $\beta(\phi)$ using the adaptive algorithm for three different initial α values

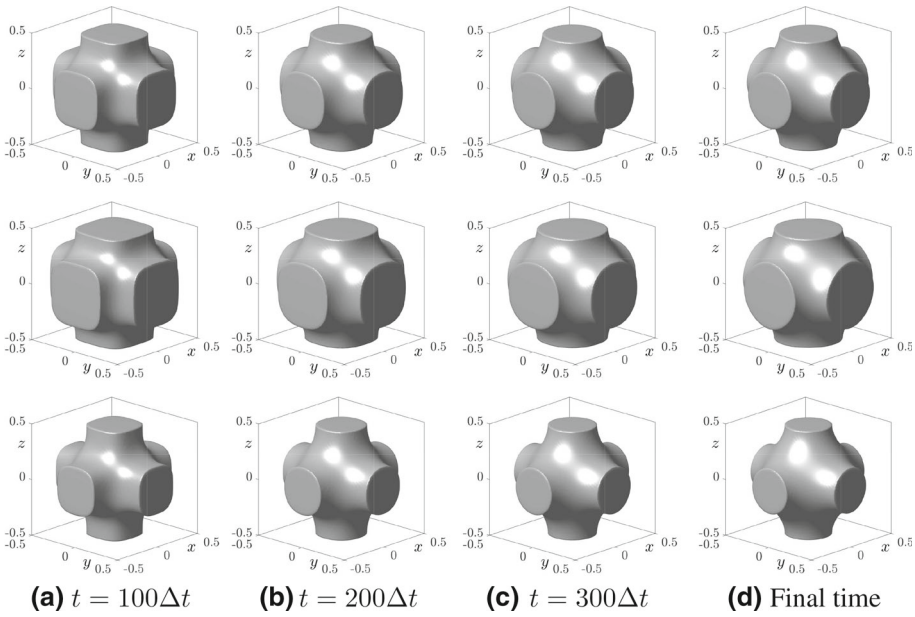

Fig. 13 Temporal evolutions with the prescribed averaged mean curvature. Times are shown below each column. From top to bottom, $\beta_T = 0,\ -1,\ 1$ and the final times are $t = 492\Delta t,\ 636\Delta t,\ 636\Delta t$, respectively

adaptively change α value in the following term in Eq. (5) according to sign of $(\beta_T - \beta(\phi^k))$:

$$\alpha(\beta_T - \beta(\phi^k))\frac{\sqrt{2F(\phi^k_{mno})}}{\epsilon}. \tag{21}$$

If $(\beta_T - \beta(\phi^k)) < 0$, then we reset $\alpha = \alpha/2$ and recompute the numerical solution; otherwise, we increase $\alpha = 1.1\alpha$ to speed up the computation of the next time update. Figure 12 shows the temporal volution of the volume $\beta(\phi)$ using the adaptive algorithm for the three different initial α values depending on the sign of $(\beta_T - \beta(\phi^k))$. We can observe the good results for all the case with initial α values, i.e., $\alpha = 5,\ 50$, and 120.

5 Conclusions

In this paper, we presented a simple and accurate computational algorithm for motion by mean curvature with constraints using a modified AC equation. The modified AC equation contains a nonlinear source term which enforces the constraints such as volume and average mean curvature. A linear convex splitting method with Fourier spectral method is used to numerically solve the modified AC equation. We performed several characteristic computational tests to demonstrate the efficiency and accuracy of the proposed algorithm. The computational results confirmed the robust and high performance of the proposed algorithm. In a future work, it would be interesting to develop an unconditionally stable scheme [12, 13, 30] using an operator splitting method. Specifically, the governing equation (1) is split into three parts: diffusion, nonlinear, and fidelity equations; and then each equation is solved by using the unconditionally stable scheme.

Acknowledgements The authors thank the reviewers for the constructive and helpful comments on the revision of this article.

Funding C. Lee was supported by the National Research Foundation of Korea(NRF) grant funded by the Korea government(MSIT) (No. 2022R1C1C2003896). H. Kim was supported by Basic Science Research Program through the National Research Foundation of Korea (NRF) funded by the Ministry of Education, Republic of Korea (NRF-2020R1A6A3A13077105). The corresponding author (J. Kim) was supported by Korea University Grant.

Availability of Data and Materials The data used to support the findings of this study are available from the corresponding author upon request.

Declarations

Conflict of interest The authors declare that they have no competing interests.

References

1. Abueidda, D.W., Al-Rub, R.K.A., Dalaq, A.S., Lee, D.W., Khan, K.A., Jasiuk, I.: Effective conductivities and elastic moduli of novel foams with triply periodic minimal surfaces. Mech. Mater. **95**, 102–115 (2016)
2. Abueidda, D.W., Bakir, M., Al-Rub, R.K.A., Bergström, J.S., Sobh, N.A., Jasiuk, I.: Mechanical properties of 3D printed polymeric cellular materials with triply periodic minimal surface architectures. Mater. Des. **122**, 255–267 (2017)
3. Abueidda, D.W., Dalaq, A.S., Al-Rub, R.K.A., Younes, H.A.: Finite element predictions of effective multifunctional properties of interpenetrating phase composites with novel triply periodic solid shell architectured reinforcements. Int. J. Mech. Sci. **92**, 80–89 (2015)
4. Abueidda, D.W., Elhebeary, M., Shiang, C.S.A., Pang, S., Al-Rub, R.K.A., Jasiuk, I.M.: Mechanical properties of 3D printed polymeric Gyroid cellular structures: experimental and finite element study. Mater. Des. **165**, 107597 (2019)
5. Afshar, M., Anaraki, A.P., Montazerian, H., Kadkhodapour, J.: Additive manufacturing and mechanical characterization of graded porosity scaffolds designed based on triply periodic minimal surface architectures. J. Mech. Behav. Biomed. Mater. **62**, 481–494 (2016)
6. Al-Ketan, O., Abu Al-Rub, R.K.: Multifunctional mechanical metamaterials based on triply periodic minimal surface lattices. Adv. Eng. Mater. **21**(10), 1900524 (2019)
7. Al-Ketan, O., Lee, D.W., Rowshan, R., Al-Rub, R.K.A.: Functionally graded and multi-morphology sheet TPMS lattices: design, manufacturing, and mechanical properties. J. Mech. Behav. Biomed. Mater. **102**, 103520 (2020)
8. Allen, S.M., Cahn, J.W.: A microscopic theory for antiphase boundary motion and its application to antiphase domain coarsening. Acta Metall. **27**(6), 1085–1095 (1979)
9. Almgren, F.J.: Minimal surface forms. Math. Intell. **4**(4), 164 (1982)

10. Andersson, S., Hyde, S.T., Larsson, K., Lidin, S.: Minimal surfaces and structures: from inorganic and metal crystals to cell membranes and biopolymers. Chem. Rev. **88**(1), 221–242 (1988)
11. Calo, V., Minev, P., Puzyrev, V.: Splitting schemes for phase-field models. Appl. Numer. Math. **156**, 192–209 (2020)
12. Chen, W., Conde, S., Wang, C., Wang, X., Wise, S.M.: A linear energy stable scheme for a thin film model without slope selection. J. Sci. Comput. **52**(3), 546–562 (2012)
13. Chen, W., Li, W., Luo, Z., Wang, C., Wang, X.: A stabilized second order exponential time differencing multistep method for thin film growth model without slope selection. EASIM Math. Model. **54**, 727–750 (2020)
14. Cheng, K., Feng, W., Wang, C., Wise, S.M.: An energy stable fourth order finite difference scheme for the Cahn–Hilliard equation. J. Comput. Appl. Math. **362**, 574–595 (2018)
15. Cheng, K., Qiao, Z., Wang, C.: A third order exponential time differencing numerical scheme for no-slope-selection epitaxial thin film model with energy stability. J. Sci. Comput. **81**, 154–185 (2019)
16. Cheng, K., Wang, C., Wise, S.M., Yue, X.: A second-order, weakly energy-stable pseudo-spectral scheme for the Cahn–Hilliard equation and its solution by the homogeneous linear iteration method. J. Sci. Comput. **69**, 1083–1114 (2016)
17. Diegel, A.E., Wang, C., Wise, S.M.: Stability and convergence of a second order mixed finite element method for the Cahn–Hilliard equation. IMA J. Numer. Anal. **36**, 1867–1897 (2016)
18. Feng, J., Fu, J., Shang, C., Lin, Z., Li, B.: Porous scaffold design by solid T-splines and triply periodic minimal surfaces. Comput. Methods Appl. Mech. Eng. **336**, 333–352 (2018)
19. Feng, X., Li, Y.: Analysis of interior penalty discontinuous Galerkin methods for the Allen–Cahn equation and the mean curvature flow. IMA J. Numer. Anal. **35**(4), 1622–1651 (2015)
20. Feng, X., Li, Y., Xing, Y.: Analysis of mixed interior penalty discontinuous Galerkin methods for the Cahn–Hilliard equation and the Hele–Shaw flow. SIAM J. Numer. Anal. **54**, 825–847 (2016)
21. Feng, X., Prohl, A.: Error analysis of a mixed finite element method for the Cahn–Hilliard equation. Numer. Math. **99**, 47–84 (2004)
22. Gandy, P.J., Bardhan, S., Mackay, A.L., Klinowski, J.: Nodal surface approximations to the P, G, D and I-WP triply periodic minimal surfaces. Chem. Phys. Lett. **336**(3–4), 187–195 (2001)
23. Guo, J., Wang, C., Wise, S.M., Yue, X.: An H^2 convergence of a second-order convex-splitting, finite difference scheme for the three-dimensional Cahn–Hilliard equation. Commu. Math. Sci. **14**, 489–515 (2016)
24. Guo, J., Wang, C., Wise, S.M., Yue, X.: An improved error analysis for a second-order numerical scheme for the Cahn–Hilliard equation. J. Comput. Appl. Math. **388**, 113300 (2021)
25. Hao, Y., Huang, Q., Wang, C.: A third order BDF energy stable linear scheme for the no-slope-selection thin film model. Commun. Comput. Phys. **29**, 905–929 (2021)
26. Jung, Y., Chu, K.T., Torquato, S.: A variational level set approach for surface area minimization of triply-periodic surfaces. J. Comput. Phys. **223**(2), 711–730 (2007)
27. Kapfer, S.C., Hyde, S.T., Mecke, K., Arns, C.H., Schröder-Turk, G.E.: Minimal surface scaffold designs for tissue engineering. Biomaterials **32**(29), 6875–6882 (2011)
28. Kim, J.: A numerical method for the Cahn–Hilliard equation with a variable mobility. Commun. Nonlinear Sci. Numer. Simul. **12**(8), 1560–1571 (2007)
29. Lee, H.G., Kim, J.: Regularized Dirac delta functions for phase field models. Int. J. Numer. Methods Eng. **91**(3), 269–288 (2012)
30. Li, W., Chen, W., Wang, C., Yan, Y., He, R.: A second order energy stable linear scheme for a thin film model without slope selection. J. Sci. Comput. **76**(3), 1905–1937 (2018)
31. Li, X., Shen, J.: Stability and error estimates of the SAV Fourier-spectral method for the phase field crystal equation. Adv. Comput. Math. **46**(3), 48 (2020)
32. Li, Y., Xia, Q., Yoon, S., Lee, C., Lu, B., Kim, J.: Simple and efficient volume merging method for triply periodic minimal structures. Comput. Phys. Commun. **264**, 107956 (2021)
33. Li, Y., Yu, Q., Fang, W., Xia, B., Kim, J.: A stable second-order BDF scheme for the three-dimensional Cahn–Hilliard–Hele–Shaw system. Adv. Comput. Math. **47**(1), 3 (2021)
34. Liu, Z., Li, X.: Step-by-step solving schemes based on scalar auxiliary variable and invariant energy quadratization approaches for gradient flows. Numer. Algorithms **89**, 65–86 (2021)
35. Liu, S., Peng, Y.: A local region-based Chan–Vese model for image segmentation. Pattern Recognit. **45**(7), 2769–2779 (2012)
36. Longley, W., McIntosh, T.J.: A bicontinuous tetrahedral structure in a liquid–crystalline lipid. Nature **303**(5918), 612–614 (1983)
37. Lu, Y., Zhao, W., Cui, Z., Zhu, H., Wu, C.: The anisotropic elastic behavior of the widely-used triply-periodic minimal surface based scaffolds. J. Mech. Behav. Biomed. Mater. **99**, 56–65 (2019)

38. Nissen, H.U.: Crystal orientation and plate structure in echinoid skeletal units. Science **166**(3909), 1150–1152 (1969)
39. Ranner, T.: A stable finite element method for low inertia undulatory locomotion in three dimensions. Appl. Numer. Math. **156**, 422–445 (2020)
40. Schwarz, H.A.: Gesammelte Mathematische Abhandlung, vol. 1. Springer, Berlin (1890)
41. Yan, Y., Chen, W., Wang, C., Wise, S.M.: A second-order energy stable BDF numerical scheme for the Cahn–Hilliard equation. Commun. Comput. Phys. **23**, 572–602 (2018)
42. Yang, J., Du, Q., Zhang, W.: Uniform L^p-bound of the Allen–Cahn equation and its numerical discretization. Int. J. Numer. Anal. Mod. **15**(1–2), 213–227 (2018)
43. Yang, S.D., Lee, H.G., Kim, J.: A phase-field approach for minimizing the area of triply periodic surfaces with volume constraint. Comput. Phys. Commun. **181**(6), 1037–1046 (2010)
44. Ye, X.C., Lin, X.C., Xiong, J.Y., Wu, H.H., Zhao, G.W., Fang, D.: Electrical properties of 3D printed graphite cellular lattice structures with triply periodic minimal surface architectures. Mater. Res. Express **6**(12), 125609 (2019)
45. Yoo, D.J.: Advanced porous scaffold design using multi-void triply periodic minimal surface models with high surface area to volume ratios. Int. J. Precis. Eng. Manuf. **15**(8), 1657–1666 (2014)
46. Yoo, D.J.: Computer-aided porous scaffold design for tissue engineering using triply periodic minimal surfaces. Int. J. Precis. Eng. Manuf. **12**(1), 61–71 (2011)
47. Yoo, D.J.: Porous scaffold design using the distance field and triply periodic minimal surface models. Biomaterials **32**(31), 7741–7754 (2011)
48. Zhang, H., Yan, J., Qian, X., Gu, X., Song, S.: On the maximum principle preserving and energy stability of high-order implicit-explicit Runge–Kutta schemes for the space-fractional Allen–Cahn equation. Numer. Algorithms **88**, 1309–1336 (2021)
49. Zhang, X.Y., Yan, X.C., Fang, G., Liu, M.: Biomechanical influence of structural variation strategies on functionally graded scaffolds constructed with triply periodic minimal surface. Addit. Manuf. **32**, 101015 (2020)